

## Methoxylated Quinoline-Chalcones with Potential Pesticidal Activity: From Synthesis to Supramolecular Framework

Antônio S. N. Aguiar,<sup>1b</sup>\*<sup>a</sup> João P. M. Rodrigues,<sup>a</sup> Leonardo L. Borges,<sup>a</sup> Wesley F. Vaz,<sup>b</sup>  
Giulio D. C. D'Oliveira,<sup>c</sup> Caridad N. Perez,<sup>1b</sup><sup>c</sup> and Hamilton B. Napolitano<sup>1b</sup><sup>a</sup>

<sup>a</sup>Grupo de Química Teórica e Estrutural de Anápolis, Universidade Estadual de Goiás,  
75132-903 Anápolis-GO, Brazil

<sup>b</sup>Departamento de Biotecnologia, Instituto Federal de Educação, Ciência e Tecnologia de Mato Grosso,  
78455-000 Lucas do Rio Verde-MT, Brazil

<sup>c</sup>Instituto de Química, Universidade Federal de Goiás, 74690-900 Goiânia-GO, Brazil

In this work, the molecular properties of the (*E*)-3-(4-nitrobenzylidene)-2-(4-methoxyphenyl)-2,3-dihydro-1-(phenylsulfonyl)-quinolin-4(1*H*)-one were studied, both in a solid and isolated state. The effect of changing the substituent groups –OCH<sub>3</sub> and –Cl in the phenyl portion was verified, where the structural and electronic properties were compared. The density functional theory was employed using the hybrid exchange-correlation functional with long-range correction M06-2X, combined with the polarized and diffuse basis set 6-311++G(d,p), in the gas phase. The electronic structure was also analyzed by frontier molecular orbitals and molecular electrostatic potential maps, where information about its chemical reactivity was obtained. Also, the supramolecular arrangement was analyzed by Hirshfeld surface (HS), 2D fingerprint plots, and quantum theory of atoms in molecules (QTAIM). The natural bond orbitals (NBO) calculations were carried out to analyze the stability and hyperconjugation energy. Finally, molecular docking was carried out to investigate the affinities of the quinoline-chalcone with a bacterial protein (*Agrobacterium pathogens*) and an ecdysone receptor-potential pesticidal activity. The results encourage further *in vitro* and *in vivo* analyses of the two kinds of organisms investigated.

**Keywords:** quinoline-chalcones, X-ray diffraction, Hirshfeld surface, density functional theory

### Introduction

Hybrid compounds between quinolines and chalcones are widely studied due to their biological potential.<sup>1-5</sup> Characterized by its heterocyclic nitrogenous nature and formed by the union of a benzene ring and a pyrimidine, quinoline,<sup>6</sup> when associated with a chalcone chain, the  $\alpha,\beta$ -unsaturated ketone aromatic system,<sup>7</sup> can exhibit diverse biological effects,<sup>1-5</sup> ranging from antibiotics,<sup>8</sup> cytotoxics,<sup>3</sup> antimalarials,<sup>9</sup> antioxidants,<sup>4</sup> anti-inflammatories,<sup>10</sup> anticancer,<sup>11</sup> and even as pesticides.<sup>12,13</sup> Moreover, it displays interest from the scientific community due to its potential as a substrate for new bioactive compounds through specific chemical changes.<sup>14</sup>

The quinoline-chalcone pesticidal effect has shown to be promising due to their natural origin, as they are

used to control weeds,<sup>15</sup> insects,<sup>16</sup> and microorganisms<sup>10</sup> harmful to agriculture, especially in more sensitive crops such as fruits and vegetables. Playing a fundamental role in agricultural production, pesticide use is unquestionable regarding efficiency and food needs. However, its toxicity and environmental pollution still need attention from researchers.<sup>17</sup> Therefore, a new biodegradable compound with a lower environmental impact is essential for society regarding environmental protection and sustainability.

In this work, the quinoline-chalcone (*E*)-3-(4-nitrobenzylidene)-2-(4-methoxyphenyl)-2,3-dihydro-1-(phenylsulfonyl)-quinolin-4(1*H*)-one (CNP-OM) was analyzed and compared to a similar compound (*E*)-3-(4-nitrobenzylidene)-2-(4-chlorophenyl)-2,3-dihydro-1-(phenylsulfonyl)-quinolin-4(1*H*)-one<sup>13</sup> (CNP-CL). The effect of the *para*-substituent groups –OCH<sub>3</sub> and –Cl on the phenyl portion was described on a structural and electronic basis. For this, theoretical calculations based on density functional theory (DFT) were carried out. Then, the intermolecular

\*e-mail: toninho.quimica@gmail.com

Editor handled this article: Paula Homem-de-Mello (Associate)



interaction patterns of both compounds were verified by Hirshfeld surfaces (HS) and 2D fingerprint plots, quantum theory of atoms in molecules (QTAIM), and natural bond orbitals (NBO) to evaluate their respective natures and stabilities in the supramolecular arrangement. Molecular docking was carried out to investigate the affinities of CNP-OM with a bacterial protein (periplasmic binding protein, present in *Agrobacterium* pathogens) and an ecdysone receptor in *Bemisia tabaci* (insecticide potential).

## Experimental

### General procedures

Nuclear magnetic resonance (NMR) spectra were collected using a Bruker Avance III 500 spectrometer (Rheinstetten, Germany) operating at 11.75 T. The spectrometer observed  $^1\text{H}$  at a frequency of 500.13 MHz and  $^{13}\text{C}$  at 125.76 MHz. A 5 mm inverse-detection three-channel ( $^1\text{H}$ ,  $^2\text{H}$ ,  $^{13}\text{C}$ , and XBB) probe and a 5 mm broadband observe (BBO) probe were utilized for the measurements. The samples, weighing approximately 10 mg, were dissolved in 600  $\mu\text{L}$  of deuterated chloroform ( $\text{CDCl}_3$ ), with tetramethylsilane (TMS) serving as the internal standard. Signal assignments were accomplished through correlation spectroscopy (COSY), heteronuclear multiple bond correlation (HMBC), and heteronuclear single quantum correlation (HSQC) experiments.

The purity of the compounds was determined based on the  $^1\text{H}$  spectra by analyzing the proportion of areas between the assigned peaks corresponding to the structure of the compound and the total area encompassing all peaks attributed to the studied material. The melting points were determined using a melting point apparatus (Karl Kolb, Frankfurt a.M., Germany) by placing the solid sample on glass coverslips and subjecting it to heating.

### Synthesis and crystallization

The synthesis of the CNP-OM<sup>18,19</sup> was undertaken using precursor **1**<sup>19</sup> (1.0 mmol) and 4-nitro-benzaldehyde (2.0 mmol) (Scheme 1). Both were dissolved in 15 mL of basic ethanol (56.1 mg of potassium hydroxide dissolved)

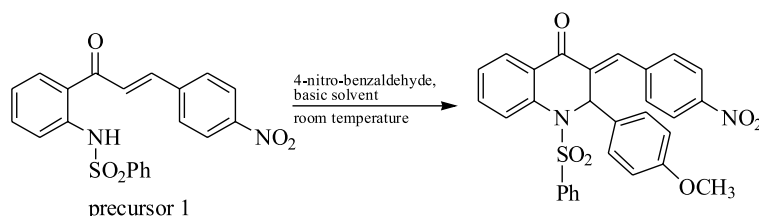
and reacted (at 25 °C) for 48 h. The solution was filtered, and the precipitate was rinsed with 15 mL of ethanol. The precipitate was dissolved in dichloromethane (10 mL), and this solution was extracted with water. The organic phase was allowed to evaporate slowly, yielding a yellow crystalline solid product with 97.8% purity.

Pale yellow crystalline solid, yield 47.5%, purity of 98.4%, mp 166-167 °C;  $^1\text{H}$  NMR (500 MHz,  $\text{CDCl}_3$ )  $\delta$  3.74 (s,  $^3\text{H}$ ), 6.57 (s,  $^1\text{H}$ ), 6.78-6.81 (m,  $^2\text{H}$ ), 7.10-7.13 (m,  $^4\text{H}$ ), 7.19-7.23 (m,  $^2\text{H}$ ), 7.28-7.33 (m,  $^3\text{H}$ ), 7.37-7.40 (m,  $^2\text{H}$ ), 7.49 (tt,  $J$  1.23, 7.48 Hz,  $^1\text{H}$ ), 7.53 (s,  $^1\text{H}$ ), 7.55 (ddd,  $J$  1.65, 7.38, 8.18 Hz,  $^1\text{H}$ ), 7.71 (dd,  $J$  0.80, 8.15 Hz,  $^1\text{H}$ ), 7.89 (dd,  $J$  1.58, 7.83 Hz,  $^1\text{H}$ );  $^{13}\text{C}$  NMR (126 MHz,  $\text{CDCl}_3$ )  $\delta$  55.2, 59.6, 114.3, 127.2, 127.3, 127.9, 128.3, 128.4, 128.7, 128.8, 128.9, 129.4, 131.2, 131.3, 132.1, 133.2, 134.7, 136.4, 137.5, 138.6, 138.9, 159.6, 182.7; IR (KBr) 1671 (m), 1605 (m), 1475 (w), 1355 (s), 1303 (m), 1253 (m) (Figure S1, Supplementary Information section); HRMS calcd. for  $\text{C}_{29}\text{H}_{23}\text{ClNO}_4\text{S}$ : 516.1036, found: 516.0902.

The first step of this reaction is the intramolecular addition of the nitrogen of the sulfonamide group to the  $\beta$  carbon of precursor **1**, followed by the reaction of the  $\beta$  carbonyl of the quinolinone formed to the aldehyde employing Claisen-Schmidt condensation, yielding the desired compounds. The CNP-OM obtained is a yellow crystalline solid with 74.1% purity. To get a single crystal for an X-ray diffraction study, a sample of the compounds was further purified by recrystallization by dissolving them in dichloromethane and exposing them to ethyl ether vapor.

### X-ray diffraction analysis

The single crystal X-ray diffraction measurements were performed in a Bruker APEX II CCD Mo  $\text{K}\alpha$  radiation diffractometer ( $\lambda = 0.71073 \text{ \AA}$ ), at a temperature of 120 K. The programs ShelXT<sup>20</sup> and SHELXL<sup>21</sup> were used to solve (direct method) and refine the structure carried out with Olex2 platform.<sup>22</sup> All hydrogen atoms were placed in calculated positions and refined with fixed individual displacement parameters [U iso (H) = 1.2Ueq or 1.5Ueq] using the riding model. CNP-OM molecular structure was verified and compared to the CNP-CL structure, also synthesized in our group.<sup>13</sup> Compound structures were



**Scheme 1.** Conditions for the synthesis of chalcone-quinolinone compounds.

deposited at Cambridge Crystallographic Data Centre (CCDC) under codes 2241212 (CNP-OM) and 1981002 (CNP-CL).

### Molecular modeling

Theoretical calculations were carried out by DFT<sup>23,24</sup> (implemented in the Gaussian16<sup>25</sup> software package) using the hybrid exchange and correlation functional with long-range correction, M06-2X,<sup>26</sup> combined with the basis set 6-311++G(d,p), in the gas phase. The geometric parameters obtained were compared to the experimental ones. The substituent groups –OCH<sub>3</sub> and –Cl of the aromatic B ring (Figure 1) are considered electron-withdrawing. Their molecular configurations were analyzed using electron density distributions from solid-state conformations. Frontier molecular orbitals<sup>27</sup> (the highest occupied molecular orbital (HOMO) and the lowest unoccupied molecular orbital (LUMO)) were obtained, and quinoline-chalcone chemical reactivity indices were determined. Molecular electrostatic potential maps<sup>28</sup> (MEP) contributed to analyzing global electrophilicity through their electronic isodensity surfaces. The electrostatic potential  $V(\mathbf{r})$ <sup>29</sup> at the point  $\mathbf{r}$  is defined as equation 1.

$$V(\mathbf{r}) = \sum_{\alpha} \frac{Z_{\alpha}}{|\mathbf{r}_{\alpha} - \mathbf{r}|} - \int \frac{\rho'(\mathbf{r}')}{|\mathbf{r}' - \mathbf{r}|} d\mathbf{r}' \quad (1)$$

where  $Z_{\alpha}$  is the charge of nuclei  $\alpha$  at point  $\mathbf{r}_{\alpha}$  and  $\rho(\mathbf{r}')$  is the charge density at the point  $\mathbf{r}'$ .<sup>28</sup> Furthermore, from the MEP map, it is possible to predict the possible regions where intermolecular interactions occur.

### Supramolecular arrangement

In supramolecular chemistry, it is possible to understand the geometric parameters formed in crystalline structures by analyzing the intermolecular interactions between molecules (or ions), regardless of the structural nature of the molecular systems.<sup>30,31</sup> The supramolecular arrangements of the quinoline-chalcones were evaluated by HS<sup>32</sup> and 2D fingerprint plots,<sup>33</sup> implemented in the CrystalExplorer software,<sup>34,35</sup> providing information about the intermolecular interaction patterns by color mapping, in addition to describing the surface-specific properties. The HS is a computational approach used to analyze and visualize the electron density distribution based on Hirshfeld partitioning, which divides the electron density of a crystal into individual atomic contributions. Once the molecular electron density is calculated using quantum mechanical methods (DFT or Hartree-Fock), it

is partitioned by assigning respective electron densities to each atom in the solid-state structure.<sup>36</sup>

$$W(\mathbf{r}) = \frac{\rho_{\text{molecule}}(\mathbf{r})}{\rho_{\text{crystal}}(\mathbf{r})} \quad (2)$$

Once the partitioning is complete, the HS is constructed by plotting the molecular surface in three dimensions, where the surface points represent equal HS values. These color-coded surface points provide information about the nature and strength of intermolecular interactions. The HS fingerprint provides a detailed distribution of interatomic contacts, revealing the relative contributions of different atoms to the overall crystal packing.<sup>33,37</sup>

Furthermore, QTAIM<sup>38,39</sup> calculations showed these interactions' characteristics through the topological parameters analysis. The inputs were constructed from the crystallographic data at the M06-2X/6-311++G(d,p) level of theory, in which the atomic coordinates were kept fixed during the calculations, and the topological parameters were obtained using the Multiwfn program.<sup>40</sup> Then, NBO<sup>41,42</sup> calculations were carried out to determine the stability of interactions by the hyperconjugation energy,<sup>43</sup> estimated by the second-order perturbation formula, equation 3.

$$E_{i \rightarrow j}^{(2)} = -n_{\sigma} \frac{\langle \sigma_i | \hat{F} | \sigma_j^* \rangle^2}{\epsilon_j^* - \epsilon_i} = -n_{\sigma} \frac{F_{ij}^2}{\epsilon_j^* - \epsilon_i} \quad (3)$$

where  $\langle \sigma_i | \hat{F} | \sigma_j^* \rangle$  or  $F_{ij}$ <sup>2</sup> is the Fock matrix element between the NBO  $i$ , and  $j$ ;  $\epsilon_{\sigma^*}$  is the energy of the antibonding orbital  $\sigma^*$  and  $\epsilon_{\sigma}$  is the energy of the bonding orbital  $\sigma$ ;  $n_{\sigma}$  stands for the population occupation of the  $\sigma$  donor orbital.

### Molecular docking

The molecular interactions of CNP-OM used to inhibit targets were studied by GOLD Suite 5.7.0<sup>44</sup> (Mark Thompson and Planaria Software LLC). The optimized structure was docked at the active site of two targets: PBP, present in *Agrobacterium tumefaciens*,<sup>45</sup> and ecdysone receptor, present in *Bemisia tabaci*.<sup>46</sup> The coordinates of these proteins were extracted from the crystal structures found in the RCSB Protein Databank<sup>47</sup> (PDB) under the PDB IDs 5ORG and 1Z5X, respectively. The 2D interaction maps were produced using the PoseView Interface.<sup>48-50</sup> PyMOL Molecular Graphics System 2.0<sup>51</sup> software was employed to build 3D images. Redocking was carried out using the structures in which the target protein and its ligands were co-crystallized. Default values were employed for all other parameters, and arrangements were submitted to 10 genetic algorithm runs using the CHEMPLP fitness function.

## Results and Discussion

### Molecular modeling analysis

The CNP-OM carbonic chain consists of five nuclei, four of which are aromatic (A, B, D, and E) and one pyrimidine (C), so that the chalcone scaffold comprises rings B and D. The nuclei B and C are condensed in the form of quinoline, and a sulfonyl group,  $-(SO_2)-$ , connects the A ring to the quinoline through a bond with the quinolinic nitrogen atom. The E ring is also connected to the quinoline portion by the bond with the chiral carbon atom,  $C_1$ . In the *para* position, there is a methoxy substituent group,  $-OCH_3$ . Figure 1 shows the CNP-OM molecular structure. The *S* enantiomer was used for the molecular modeling analysis. The CNP-OM crystallized on monoclinic crystal system  $C2/c$ , with the following crystallographic parameters:  $a = 22.469(2)$  Å,  $b = 15.387(2)$  Å,  $c = 15.4935(18)$  Å,  $\alpha = 90^\circ$ ,  $\beta = 108.456(3)^\circ$ ,  $\gamma = 90^\circ$  and  $V = 5081.07$  Å<sup>3</sup>. The substitution of the  $-OCH_3$  group by the  $-Cl$  group in the *E* ring changes the crystalline environment and space group symmetry.<sup>13</sup> Crystallographic data from refinement and data collection for the quinoline-chalcones CNP-OM and CNP-CL are shown in Table 1.

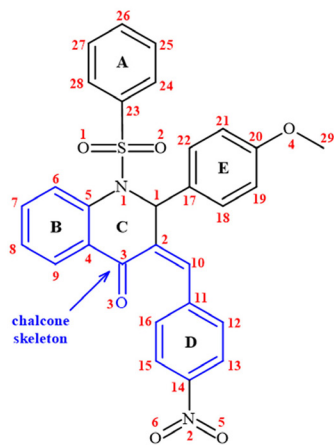


**Figure 1.** CNP-OM quinoline-chalcone molecule.

The molecular geometries of the compounds do not show significant differences, despite the different substituent groups. For bond lengths, it was observed that  $C_{27}-C_{28}$  (ring A),  $N_2=O_5$  ( $-NO_2$  group), and  $C_{19}-C_{20}$  bonds are larger in CNP-CL by about 1.67, 1.24, and 1.24%, respectively. The latter is due to the steric effect caused by the  $-OCH_3$  group on the benzene ring. Since the Cl atom is bulky, the  $C_{20}-Cl$  bond is 21.1% larger than the  $C_{20}-O_4$  bond in CNP-OM. In CNP-OM, the  $C_{20}-O_4$  bond is of the order of a  $-C=C-$  bond on the benzene ring. This is because the  $O_4$  lone pairs resonate with the  $\pi$  electrons of the

**Table 1.** Crystallographic data and structure refinement for CNP-OM and CNP-CL

Crystal data	CNP-OM	CNP-CL
Chemical formula	$C_{29}H_{22}N_2O_6S$	$C_{28}H_{19}N_2O_5ClS$
Molecular weight / (g mol <sup>-1</sup> )	526.60	530.96
Crystal system	monoclinic	monoclinic
Space group	$C2/c$	$P2_1/n$
$a$ / Å	22.469(2)	11.1075(4)
$b$ / Å	15.387(2)	14.4637(5)
$c$ / Å	15.4935(18)	15.2820(5)
$\alpha$ / degree	90	90
$\beta$ / degree	108.456(3)	96.658(4)
$\gamma$ / degree	90	90
Volume / Å <sup>3</sup>	5081.1(11)	2338.58(16)
Z	8	4
Radiation type	Mo K $\alpha$ ( $\lambda = 0.71073$ )	Mo K $\alpha$ ( $\lambda = 0.71073$ )
R[F2 > 2 $\sigma$ (F2)]	0.0431	0.0428
wR(F2)	0.1069	0.1165
S	1.027	1.029

$a$ - $c$  and  $\alpha$ - $\gamma$ : unit cell parameters; Z: number of formula units *per* cell; wR(F2): weighted-profile R-factor; S: goodness of fit from least-squares minimization function.

aromatic ring, balancing the bond distance. The resonance effect does not occur with the  $-Cl$  atom, leaving only the steric effect, which lengthens the bond. For bond angles, it was observed that the  $C_1-C_{17}-C_{18}$  angle is greater in the CNP-OM, around 1.52%, and the  $N_1-S-C_{23}$ ,  $C_2=C_{10}-C_{11}$ ,  $C_{15}-C_{14}-N_2$ ,  $C_{19}-C_{20}-C_{21}$ , and  $C_1-C_{17}-C_{22}$  angles are smaller, respectively, 1.82, 1.35, 1.22, 1.41, and 1.21%, compared to the CNP-CL. In Figure 2, it is possible to observe that the geometric parameters are homogeneous. The A, B, D, and E rings are plane in both compounds. The  $C_3$  and  $N_1$  atoms are in the same plane of the B ring; however, the carbonyls of the chalcone chains are  $12.76^\circ$  out of this plane in CNP-OM and  $16.66^\circ$  in CNP-CL, a difference of ca. 30%. Furthermore, rings B and D are at  $47.49^\circ$  in CNP-OM and  $26.44^\circ$  in CNP-CL, while rings B and E are almost perpendicular ( $81.77^\circ$  in CNP-OM and  $73.17^\circ$  in CNP-CL). Finally, the S atom of the sulfonyl group is  $7.08^\circ$  out of the plane of the A ring in CNP-OM, while it is  $2.88^\circ$  in CNP-CL.

The theoretical geometric parameters were compared to the experimental data through the mean absolute deviation percentage (MADP), equation 4.

$$MADP = \frac{100}{n} \sum_{i=1}^n \left| \frac{\chi_{DFT} - \chi_{XRD}}{\chi_{XRD}} \right| \quad (4)$$

where  $\chi_{DFT}$  and  $\chi_{XRD}$  represent the theoretical and experimental geometric parameters, respectively. The

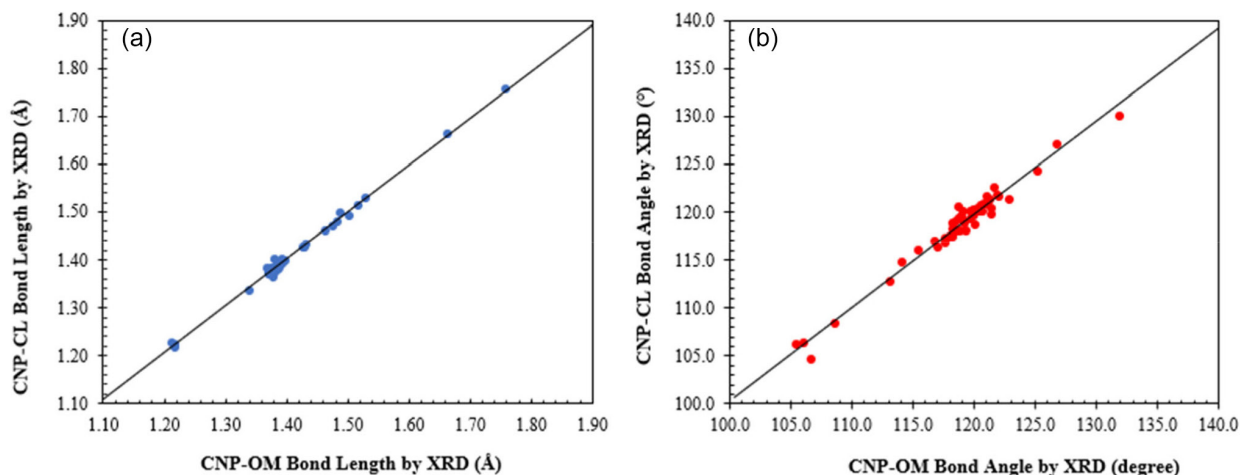


**Figure 2.** Scatter plots comparing experimental values of bond lengths (a) and bond angles (b) in CNP-OM and CNP-CL quinoline-chalcones.

results showed that the theory level used could well describe the quinoline-chalcone molecular structures. MADP values for bond lengths were 0.718% in CNP-OM,

with Pearson's correlation coefficient,  $R^2 = 0.9936$ , and 0.645% in CNP-CL, with  $R^2 = 0.9967$ . Figure 3 shows the graphs for the theoretical geometric parameters compared

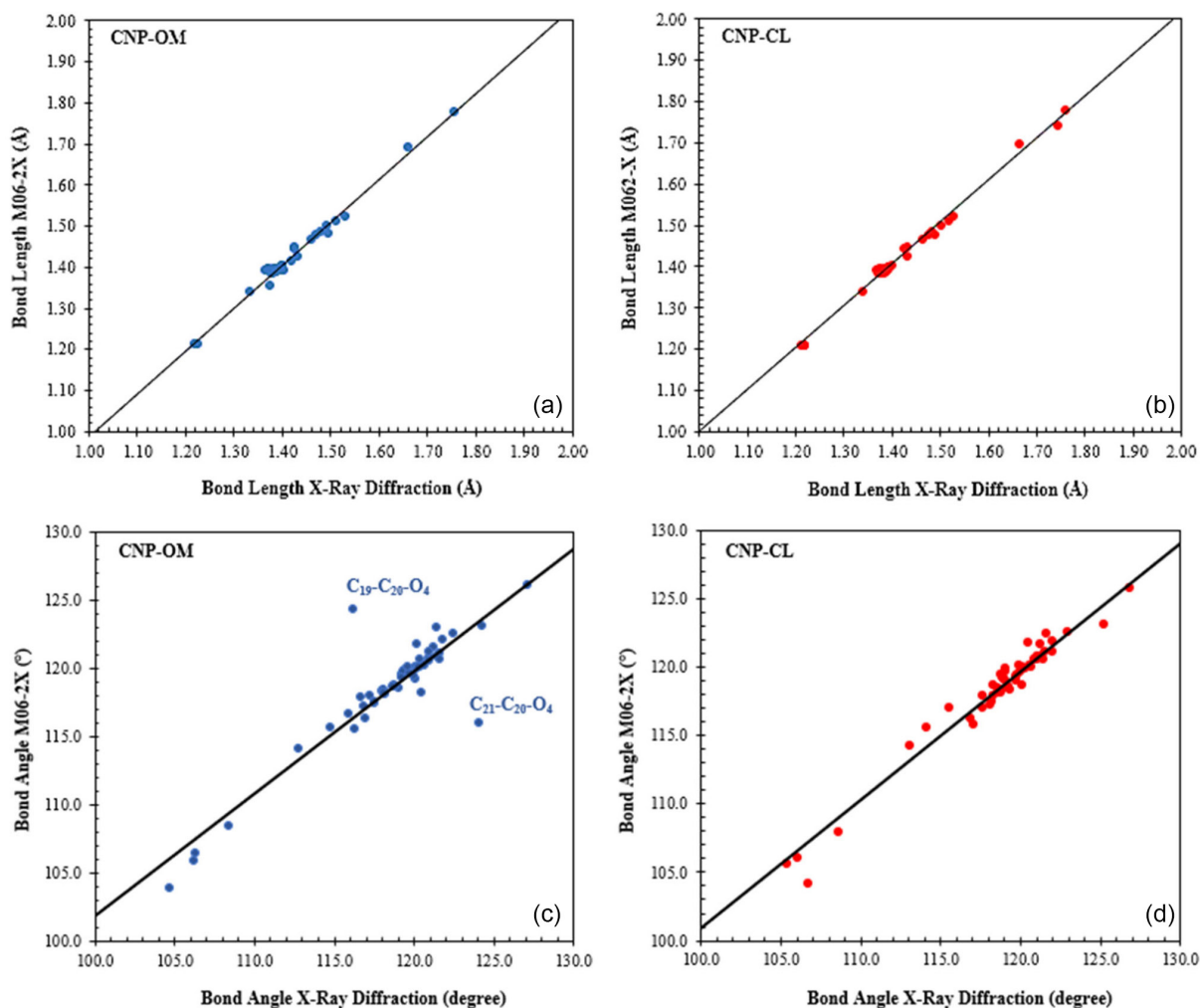


**Figure 3.** Scatter plots comparing experimental and theoretical values of the bond lengths (a) and (b), and bond angles (c) and (d) in CNP-OM and CNP-CL quinoline-chalcones.

to the experimental ones. In the case of bond angles, the MADP values were 0.680% ( $R^2 = 0.9229$ ) for CNP-OM and 0.588% ( $R^2 = 0.9780$ ) for CNP-CL.

The data showed that the dihedral angles undergo minor changes in the CNP-OM molecule, depending on the molecular environment; moreover, the superposition of the CNP-OM structure in the crystal and isolated form showed that the  $-OCH_3$  group can rotate in different environments (Figure 4a). On the other hand, in the CNP-CL molecule, the torsional variation is greater when compared to the settings described above; however, the values of their dihedrals changed in a non-significant way compared to the experimental data (Figure 4b).

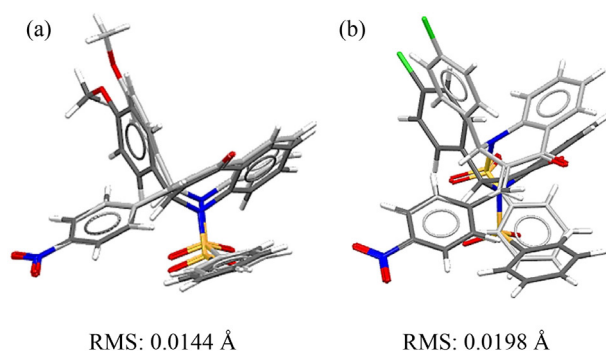


**Figure 4.** CNP-OM (a) and CNP-CL (b) overlapping molecular structures, where molecules with C atoms in light gray correspond to the crystal and molecules with C atoms in dark gray correspond to theoretical calculations.

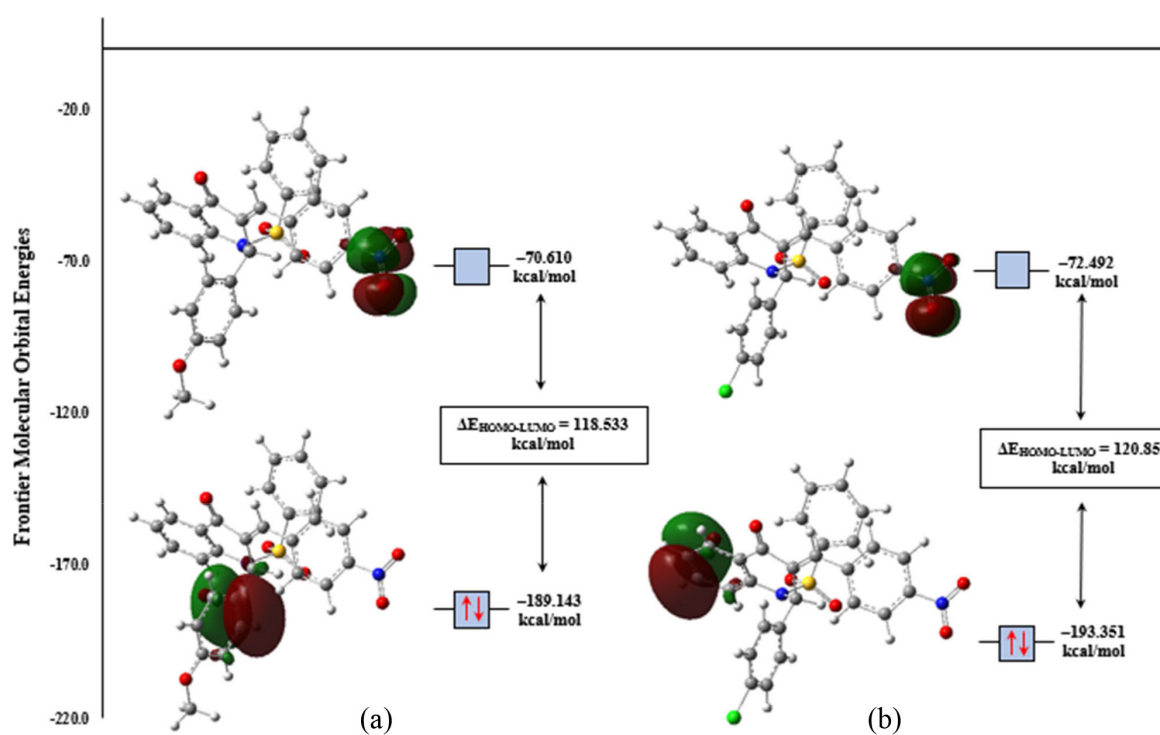


**Figure 5.** HOMO and LUMO plots for (a) CNP-OM and (b) CNP-CL obtained at M06-2X/6-311++G(d,p) level of theory.

The electron density function  $\rho(\mathbf{r})$  is very useful in modeling the chemical behavior of molecules,<sup>24,52-54</sup> and from the results of the CNP-OM and CNP-CL quinoline-chalcone electronic structures, it was possible to predict some important information about the kinetic stability and chemical reactivity.<sup>52,54,55</sup> According to Pearson's Principle,<sup>56,57</sup> compounds that exhibit an acidic character have low LUMO energies, while compounds with a basic character have high HOMO energies. Thus, it is expected that the electron-withdrawing effect of the  $-OCH_3$  group gives the CNP-OM molecule a more basic character than CNP-CL, even with the electron-withdrawing group  $-Cl$ .

The isosurfaces of the localized FMOs (HOMO and LUMO) obtained for the compounds are shown in Figure 5, and their energy values are shown in Table 2. From the results, the HOMO energy in CNP-OM is about 2.2% higher, and the LUMO energy is about 2.6% lower compared to CNP-CL. In CNP-OM, HOMO is located at the  $C_{17}-C_{18}$  bond and has a bonding  $\pi$  character. This orbital has an occupancy of 1.67e, formed by the contribution of 54.28% of the  $p$  orbital of  $C_{17}$  and 45.72% of the  $p$  orbital of  $C_{18}$ , perpendicular to the plane of the benzene ring. Due to the slightly higher HOMO value, CNP-OM has a slightly higher basic character. The HOMO of CNP-CL is also a bonding  $\pi$  orbital with occupancy 1.62e, located in the  $C_7-C_8$  bond and formed by the contribution of 48.51% of the  $p$  orbital of  $C_7$  and 51.49% of the  $p$  orbital of  $C_8$ . On the other hand, the lower LUMO energy value in CNP-CL

**Table 2.** Reactivity indices for CNP-OM and CNP-CL compounds obtained at M06-2X/6-311++G(d,p) level of theory

Descriptor	CNP-OM / (kcal mol <sup>-1</sup> )	CNP-CL / (kcal mol <sup>-1</sup> )
E <sub>HOMO</sub>	-189.143	-193.351
E <sub>LUMO</sub>	-70.610	-72.492
ΔE <sub>H-L</sub> <sup>a</sup>	118.533	120.859
Ionization energy (I)	189.143	193.351
Electronic affinity (A)	70.610	72.492
Electronegativity (χ)	129.877	132.921
Chemical potential (μ)	-129.877	-132.921
Chemical hardness (η)	118.533	120.859
Electrophilicity index (ω)	71.153	73.094

<sup>a</sup>The energy gap is the difference between the HOMO and LUMO energies, ΔE<sub>H-L</sub> = E<sub>LUMO</sub> - E<sub>HOMO</sub>.

gives the compound a slightly acidic character. Its LUMO is an antibonding π\* orbital, with occupancy 0.59e, located in the N<sub>2</sub>=O<sub>6</sub> bond and formed by the contribution of 61.33% of the p orbital of N<sub>2</sub> and 38.67% of the p orbital of O<sub>6</sub>.

The energy gaps (ΔE<sub>H-L</sub>) are shown in Table 2. As it results in a slightly lower ΔE<sub>H-L</sub> (1.92%), the -OCH<sub>3</sub> substituent group in CNP-OM makes it a more reactive compound than CNP-CL. Chemical hardness (η)<sup>58,59</sup> calculations, equation 5, showed that the CNP-OM orbitals are 1.92% softer, so the molecule is slightly more polarizable. In addition, the values obtained for the chemical potential<sup>57</sup> of the compound, equation 6, showed that CNP-OM has a more remarkable ability to transfer electrons in chemical processes since its μ is about 2.29% higher. In equations 5, and 6, is the energy of the system, N is the number of electrons, υ is the external potential, I = -E<sub>HOMO</sub> is the ionization potential, and A = -E<sub>LUMO</sub> is the electron affinity.

$$\eta = \frac{1}{2} \left( \frac{\partial^2 E}{\partial N^2} \right)_{\nu} = \frac{I - A}{2} \quad (5)$$

$$\mu = \left( \frac{\partial E}{\partial N} \right)_{\nu} = -\frac{I + A}{2} = -\chi \quad (6)$$

From the and values calculated for the quinoline-chalcones, the global electrophilicity indices (ω)<sup>60</sup> values were obtained for the compounds, equation 7:

$$\omega = \frac{\mu^2}{2\eta} \quad (7)$$

which measures the electrophilic nature of a molecule. Quantitative characterization of this description was carried

out for several organic molecules,<sup>61,62</sup> in which the theoretical results showed that, for strong electrophiles, ω > 1.5 eV (or ω > 35 kcal mol<sup>-1</sup>), for moderate electrophiles, 0.8 eV < ω < 1.5 eV (or 18 kcal mol<sup>-1</sup> < ω < 35 kcal mol<sup>-1</sup>), and finally, for marginal electrophiles, ω < 0.8 eV (or ω < 18 kcal mol<sup>-1</sup>). It is possible to infer that CNP-OM and CNP-CL are strong electrophiles and that the results found were, respectively, 71.1 and 73.1 kcal mol<sup>-1</sup>.

The local electrophilicity can be obtained from the Fukui function,<sup>63,64</sup> which determines the regions of nucleophilic (f<sup>+</sup>, equation 8), electrophilic (f<sup>-</sup>, equation 9), or radical attacks (f<sup>0</sup>, equation 10).

$$f^+ = \left[ \frac{\partial \rho(r)}{\partial N} \right]_{\nu}^+ \quad (8)$$

$$f^- = \left[ \frac{\partial \rho(r)}{\partial N} \right]_{\nu}^- \quad (9)$$

$$f^0 = \left[ \frac{\partial \rho(r)}{\partial N} \right]_{\nu}^0 \quad (10)$$

The MEP maps of CNP-OM and CNP-CL (Figure 6) revealed that the regions over the oxygen atoms (in red) contain a high charge density, configuring the nucleophilic regions of the molecules. Evaluating the isosurfaces obtained for the f<sup>+</sup> function (Figure 7), we noticed that the O atoms present in the -NO<sub>2</sub>, -(CO)-, and -(SO<sub>2</sub>)- groups can carry out nucleophilic attacks during chemical processes, including the O<sub>4</sub> atom of the -OCH<sub>3</sub> group of the CNP-OM. In addition to these regions, we observed that the -OCH<sub>3</sub> substituent group in CNP-OM makes C<sub>18</sub> and C<sub>21</sub> (or C<sub>19</sub> and C<sub>22</sub>) atoms susceptible to attacks of this nature, while the -Cl substituent group in CNP-CL alters the nucleophilic attack regions to atoms C<sub>19</sub> and C<sub>20</sub> (or C<sub>20</sub> and C<sub>21</sub>). The quinoline N atom is susceptible to this type of attack, which is more pronounced in the CNP-CL structure. Finally, the unsaturated C<sub>10</sub> atom of the chalcone bridge of the chlorinated compound is susceptible to this type of attack.

Electrophilic attacks, according to the f<sup>-</sup> function isosurfaces can occur on the C<sub>29</sub> atom of the -OCH<sub>3</sub> group in CNP-OM. As the -CH<sub>3</sub> group is an electron-donating group and the O<sub>4</sub> atom is very electronegative, C<sub>29</sub> acquires a partial positive charge, making the charge density in its region low and susceptible to electrophilic attacks. The blue color in the MEP map shows that this is an electrophilic region. In the region of the -Cl substituent group, in CNP-CL, we observed that this type of attack does not occur. Electrophilic attacks can occur on C<sub>4</sub>, C<sub>5</sub>, C<sub>6</sub>, and C<sub>7</sub> atoms in the quinoline portion. Compared with the LUMO in both compounds described above, the results

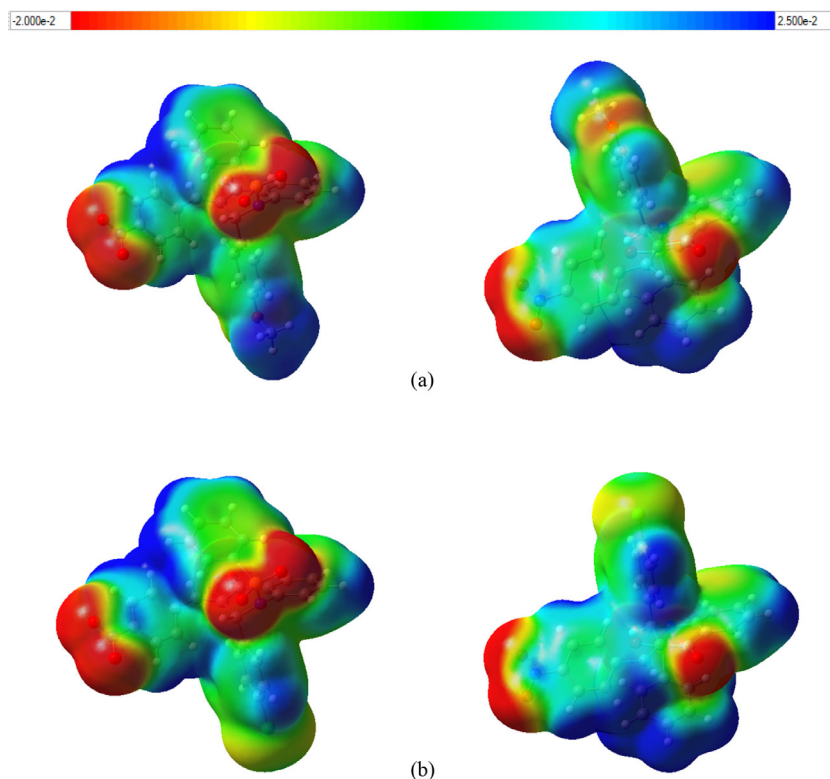


**Figure 6.** MEP surface at  $\rho(r) = 4.0 \times 10^{-4}$  electrons/Bohr contour of the total SCF electronic density for (a) CNP-OM and (b) CNP-CL at the M06-2X/6-311++G(d,p) level of theory.

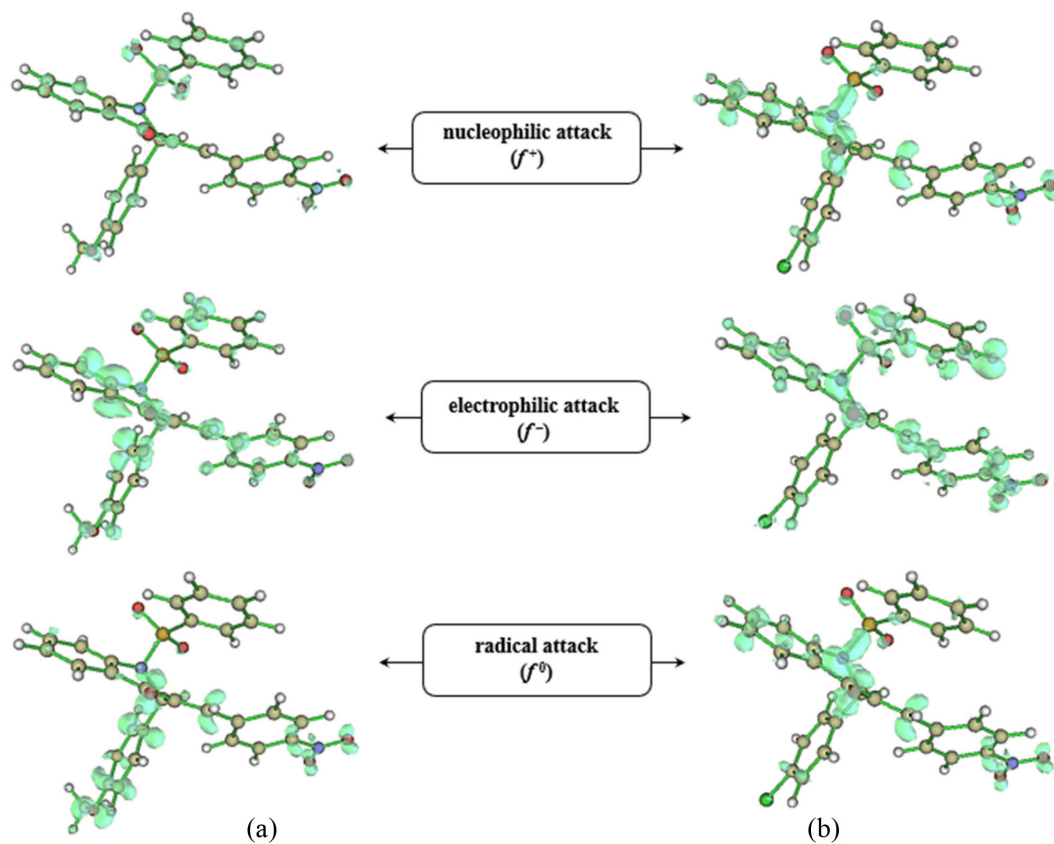


**Figure 7.** Isosurfaces of the  $f^+$ ,  $f^-$ , and  $f^0$  functions indicating the nucleophilic, electrophilic, and radical attack regions, respectively, for CNP-OM and CNP-CL molecules, obtained with isodensity 0.5.

indicate the same trend since they are regions formed by orbitals that tend to capture electrons. In the nitrobenzene ring, the C<sub>13</sub> (or C<sub>15</sub>) and C<sub>11</sub> atoms are also susceptible to electrophilic attacks since -NO<sub>2</sub> is an electron-withdrawing group, causing the minimization of the charge density on these atoms and making them electrophilic. Finally, in the A ring, the carbon atoms in the *meta*-position can undergo electrophilic attacks. However, in CNP-CL, the *ortho*-opposite position is also susceptible to this attack.

According to the isosurfaces of the  $f^0$  function, it is possible to observe that radical attacks are common throughout the chalcone core in both compounds, mainly on C<sub>10</sub> and O<sub>3</sub> atoms. Furthermore, the O<sub>5</sub> and O<sub>6</sub> atoms of the -NO<sub>2</sub> group and the C<sub>14</sub> atom of the D ring can also suffer this attack. However, changing the substituent group modified the E ring and quinoline radical attack regions in the molecules. In the case of CNP-OM, the C<sub>20</sub>, C<sub>19</sub> (or C<sub>21</sub>), and C<sub>17</sub> atoms, as well as the O<sub>4</sub> atom of the -OCH<sub>3</sub> group, are susceptible to attacks of this nature. In CNP-CL, it was observed that the sites of radical attacks were on the C<sub>7</sub>, C<sub>8</sub>, and C<sub>9</sub> atoms of the B ring and the N<sub>1</sub> atom of the quinoline.

### Supramolecular arrangement

The comparison of the CNP-OM and CNP-CL supramolecular arrangements showed that -OCH<sub>3</sub> and -Cl cause different intermolecular interaction patterns in the respective crystals. Initially, an interaction between the E ring and the -NO<sub>2</sub> group (C<sub>19</sub>-H<sub>19</sub>...O<sub>6</sub>) was observed in compounds whose distances between the H atom and the acceptor atom differed by only 0.5%, while the D-H-A angles differed by 20.3%. This difference is related to the fact that, in CNP-OM, the O ether atom also participates in the formation of dimer 1, represented by the HS<sup>32</sup> in Figure 8a. In contrast, the Cl atom in CNP-CL does not carry out other interactions in addition to the mentioned above. The quinoline portion of both compounds forms dimers: in CNP-OM, by the C<sub>9</sub>-H<sub>9</sub>...O<sub>3</sub> interaction (dimer 3), while in CNP-CL, by the C<sub>27</sub>-H...O<sub>3</sub> interaction (dimer 3). In addition to the formation of this dimer, two other chain interactions were observed in CNP-OM through contacts between the B ring and the -NO<sub>2</sub> group (C<sub>8</sub>-H<sub>8</sub>...O<sub>5</sub>) and contacts between the quinoline-ketone group and the D ring (C<sub>15</sub>-H<sub>15</sub>...O<sub>3</sub>). The A ring also participates in the formation of dimers in the compounds so that, in CNP-CL, this portion of the molecule forms a dimer through contacts with the -NO<sub>2</sub> group by the intermolecular interactions C<sub>24</sub>-H...O<sub>5</sub> and C<sub>25</sub>-H...O<sub>6</sub>; also, ring A participates in the interaction C<sub>28</sub>-H...O<sub>3</sub>. On the other hand, in CNP-OM, we observed only the formation of dimer 2 (Figure 8b) by the interaction C<sub>28</sub>-H<sub>28</sub>...O<sub>1</sub>.

There are three independent dimers of CNP-OM in the supramolecular arrangement: dimer 1 (Figure 8a) with C<sub>12</sub>-H<sub>12</sub>...O<sub>4</sub> and C<sub>13</sub>-H<sub>13</sub>...O<sub>4</sub> interactions (2.591 and 2.653 Å, respectively) described by R<sub>2</sub><sup>2</sup>(22),<sup>65,66</sup> dimer 2 (Figure 8b) with C<sub>28</sub>-H<sub>28</sub>...O<sub>1</sub> (2,589 Å) interaction described by R<sub>2</sub><sup>2</sup>(10); dimer 3 (Figure 8c) with C<sub>9</sub>-H<sub>9</sub>...O<sub>3</sub> interaction described by R<sub>2</sub><sup>2</sup>(10). In addition, other intermolecular interactions were observed in the CNP-OM: C<sub>8</sub>-H<sub>8</sub>...O<sub>5</sub>, at 2.366 Å, described by C<sub>1</sub><sup>1</sup>(13) (Figure 8d), C<sub>15</sub>-H<sub>15</sub>...O<sub>3</sub>, at 2.511 Å, described by (13) (Figure 8e), and C<sub>19</sub>-H<sub>19</sub>...O<sub>6</sub>, at 2.586 Å, described by C<sub>1</sub><sup>1</sup>(8) (Figure 8f). Furthermore, through the shape index<sup>32</sup> (Figure 9), there are two π...π stacking interactions in the CNP-OM supramolecular arrangement. The first occurs in dimer 1 due to the contact between the E rings (Figure 9a) at 4,324 Å, while the second occurs due to the contact between the D rings (Figure 9b) at 3.616 Å.

Similarly, three dimers constructed in the CNP-CL supramolecular arrangement were observed.<sup>13</sup> Dimer 1 (Figure 10a) is formed by the contacts between the O<sub>1</sub> and O<sub>2</sub> atoms of the sulfonyl group with the D ring, whose interactions C<sub>12</sub>-H...O<sub>1</sub> and C<sub>13</sub>-H...O<sub>2</sub> have lengths of 2.528 and 2.441 Å, respectively. This dimer is described by R<sub>2</sub><sup>2</sup>(18) and (20). Described by R<sub>2</sub><sup>2</sup>(28) and R<sub>2</sub><sup>2</sup>(30), dimer 2 (Figure 10b) is formed by contacts of the O<sub>5</sub> and O<sub>6</sub> atoms of the -NO<sub>2</sub> group with the A ring of the compound at 2.591 and 2.673 Å, observed by C<sub>24</sub>-H...O<sub>5</sub> and C<sub>25</sub>-H...O<sub>6</sub> interactions. In dimer 3 (Figure 10c) C<sub>27</sub>-H...O<sub>3</sub> interactions are observed, carried out by contacts between the O<sub>3</sub> atom of the quinoline-ketone group and the A ring at 2.655 Å. In this case, the dimer can be described by R<sub>2</sub><sup>2</sup>(20). Only the C<sub>19</sub>-H...O<sub>5</sub> interaction participates in chain contacts (Figure 10d) in the supramolecular arrangement of CNP-CL, described by C<sub>1</sub><sup>1</sup>(13). Finally, we observed C-H...π interactions (Figure 11) in the CNP-CL supramolecular arrangement.

2D fingerprint analysis<sup>33</sup> (Figure 12) showed that 31.8% of the HS of the quinoline-chalcone corresponds to O...H contacts, 13.4% to C...H contacts, 42.8% to H...H contacts, and only 4.9% to C...C contacts. The latter is related to the π...π stacked contacts observed in dimer 1. The analysis of the 2D fingerprint plots of both compounds showed that replacing the Cl group by -OCH<sub>3</sub> increased the area of O...H and H...H type contacts by 26.2 and 25.9% on the HS of CNP-OM, respectively. Likewise, C-C contacts increased by almost 2.5 times. However, the number of C...H contacts is about 19.8% lower in CNP-OM. Figure 12c shows the CNP-OM fingerprint plot, and the column plot compares the contents of each contact over the HS areas in both quinoline-chalcones.

According to QTAIM,<sup>38</sup> the observable properties of a chemical system are contained in its electron density,

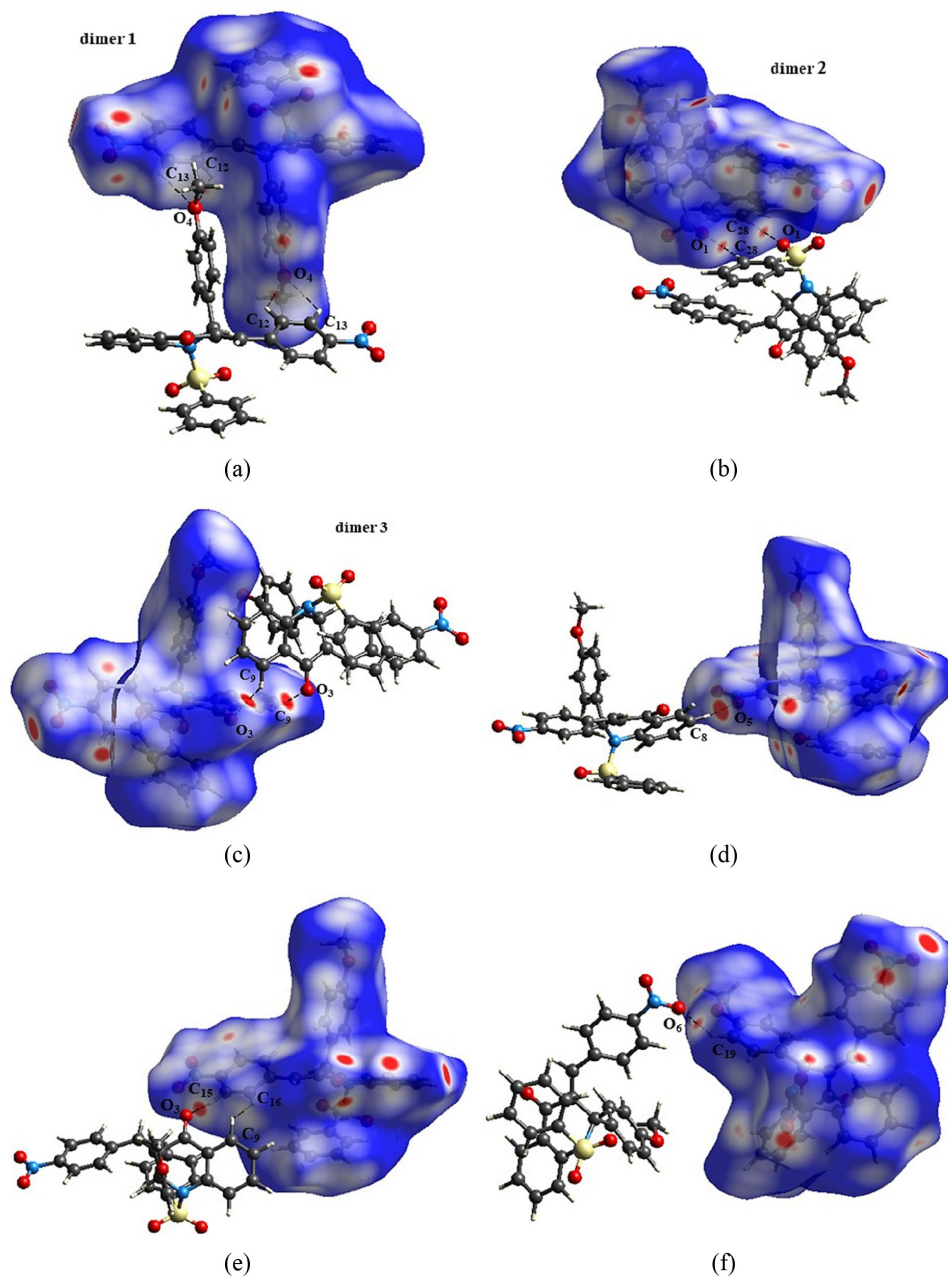


**Figure 8.** The HS  $d_{\text{norm}}$  map showing the interactions observed in the CNP-OM molecular packing.

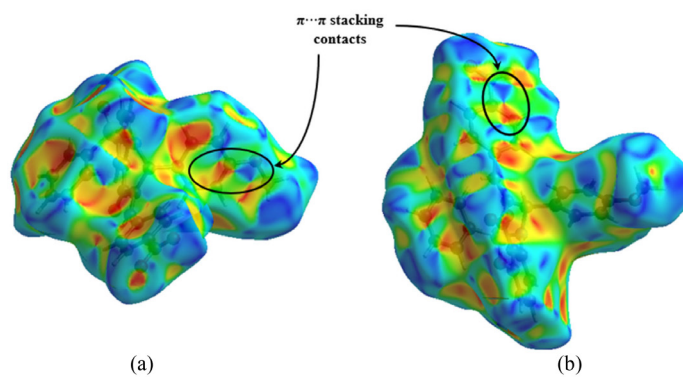


**Figure 9.** Shape index surface showing the  $\pi \cdots \pi$  stacking interactions establishing the CNP-OM crystal packing.

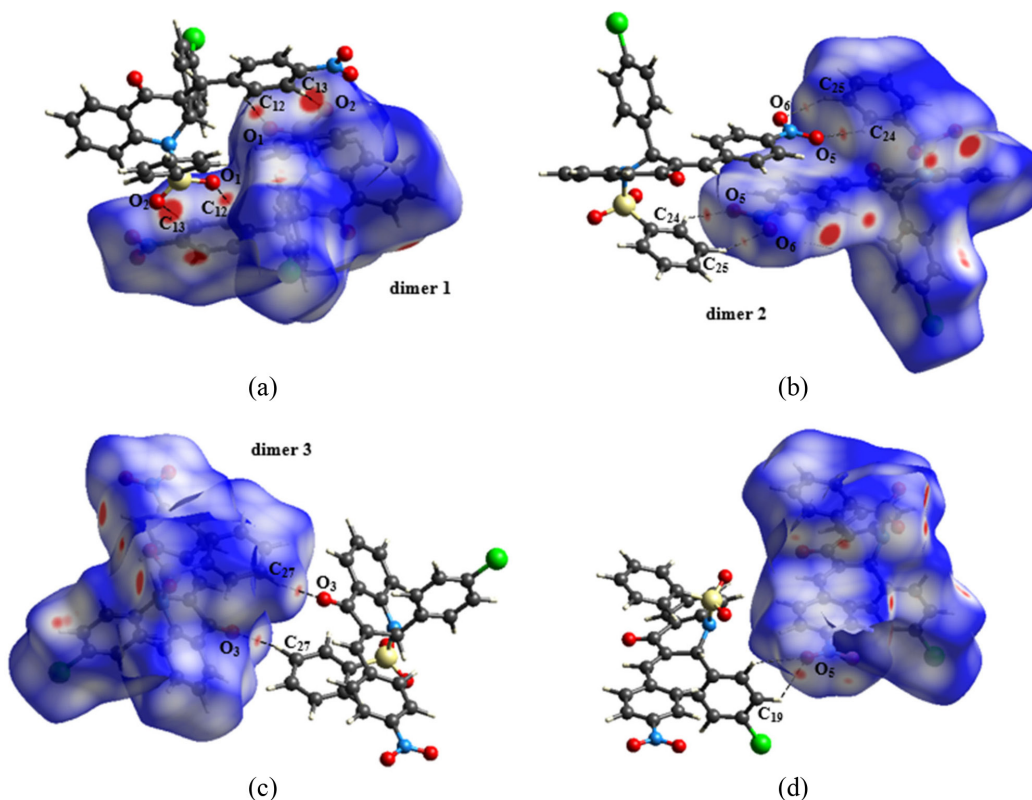


**Figure 10.** The HS  $d_{\text{norm}}$  map shows the interactions observed in the CNP-CL molecular packing.

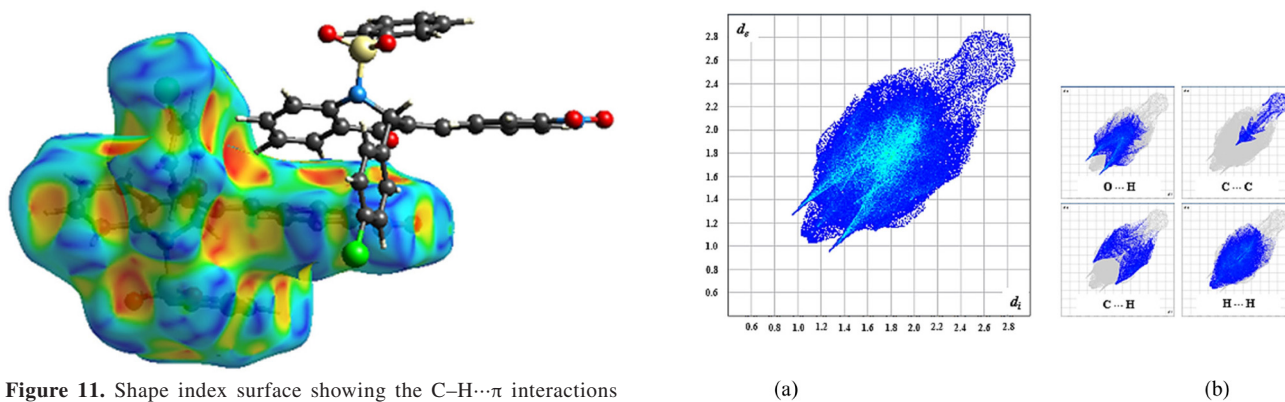


**Figure 11.** Shape index surface showing the C-H... $\pi$  interactions establishing the CNP-CL crystal packing.

$\rho(\mathbf{r})$ , so that the gradient vector of  $\rho$ ,  $\nabla\rho(\mathbf{r})$ , defines the bond paths (BP), starting from atomic nuclei (attractors). This way, points between two attractors are called bond critical points (BCP).<sup>67</sup> The Laplacian electron density determines the location of a BCP ( $\nabla^2\rho$ ), which describes the electron concentration in the BP. In shared interactions, as in a covalent bond, electrons are accumulated in the BCP, resulting in  $\nabla^2\rho < 0$ ; on the other hand, in closed-shell interactions, as in partially covalent bonds, hydrogen bonds, or van der Waals interactions, the attractors support all the charge and  $\nabla^2\rho > 0$ . After this brief description of the method and the topological parameters obtained (Table 2),

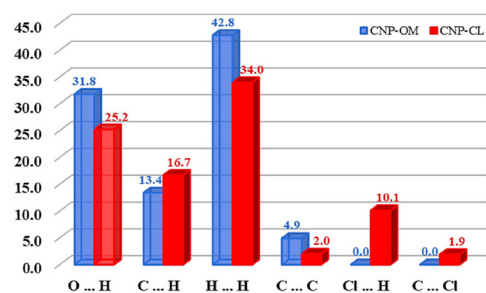


**Figure 12.** (a) 2D fingerprint plots of the nearest external distance ( $d_e$ ) versus the nearest internal distance ( $d_i$ ) for CNP-OM, and (b) the regions corresponding to O...H, C...H, C...C, and H...H contacts. The colors represent the number of points that share the same  $d_i$ ,  $d_e$  coordinate (light blue: many; dark blue: few). (c) Graph of the percentages of each contact on the HS in the quinoline-chalcones CNP-OM (blue) and CNP-CL (red).

we observe that the electron density is very low ( $\rho < 0.1$ ) between two attractors that form the intermolecular interaction in both quinoline-chalcones. Furthermore, the  $\nabla^2\rho > 0$  values indicate that electrons are depleted in the BCP, configuring closed-shell interactions.

By the virial theorem (equation 11), in atomic units, and by the equation 12, it was shown that the energetic topological parameters are related to  $\nabla^2\rho$ , where  $h(\mathbf{r})$  corresponds to the electron density energy,  $G(\mathbf{r})$  to the kinetic energy density, and  $v(\mathbf{r})$  the potential energy density.

$$\frac{1}{4}\nabla^2\rho(\mathbf{r})=2G(\mathbf{r})+v(\mathbf{r}) \quad (11)$$

$$h(\mathbf{r})=G(\mathbf{r})+v(\mathbf{r}) \quad (12)$$

For H bonds, it was shown that the intensity of the interaction is powerful for values of  $\nabla^2\rho < 0$  and  $h < 0$ , strong for values of  $\nabla^2\rho > 0$  and  $h < 0$  and weak or moderate for values of  $\nabla^2\rho > 0$  and  $h > 0$ .<sup>68</sup> In the case of interactions in the supramolecular arrangement of the quinoline-chalcones CNP-OM and CNP-CL, by analogy, the interactions are weak H-bonds. Furthermore, the values found for the ratio  $|v|/G$  showed that the potential energy density is smaller than the kinetic energy density, indicating that the internuclear electronic flux is small between the attractors, resulting in weak interactions. Molecular graphs of supramolecular arrangements are shown in

Figure 13, and only the BPs and the respective BCPs for the interactions are presented in Table 3.

The NBO analysis<sup>41,42</sup> showed that the H-bonds in both quinoline-chalcones are weakly stabilized by the hyperconjugation<sup>43</sup> of the donor orbitals (Lewis type) with the acceptor orbitals (non-Lewis type). Interactions in the supramolecular arrangement of CNP-OM occur by hyperconjugation of lone pairs of oxygen atoms or by bonding orbitals with antibonding  $\rho^*$  or  $\pi^*$  orbitals. In CNP-CL, hyperconjugations occur between lone pairs of O with antibonding  $\rho^*$  or  $\pi^*$  orbitals, except for the  $C_{27}-H\cdots O_3$  interaction. For example, dimer 1, present in the supramolecular arrangement of CNP-OM, is formed by the H-bonds  $C_{12}-H\cdots O_4$  and  $C_{13}-H\cdots O_4$ . The  $C_{12}-H\cdots O_4$  interaction is stabilized by the hyperconjugations  $\eta_1(O_4) \rightarrow \sigma^*(C_{11}-C_{12})$  and  $\eta_2(O_4) \rightarrow \sigma^*(C_{12}-H)$ , with  $E^{(2)}$  values equal to 0.16 and 0.11 kcal mol<sup>-1</sup>, respectively. In this case, the  $\eta_1(O_4)$  orbital is a  $sp^{1.60}$  hybrid that has an occupancy of 1.97e, hyperconjugated with the antibonding orbital of  $C_{11}-C_{12}$ , formed by the contribution of 49.35% of the  $sp^{1.90}$  hybrid orbital of  $C_{11}$  and 50.65% of the  $sp^{1.94}$  hybrid orbital of  $C_{12}$ , presenting an occupancy of 0.03e. The  $\eta_2(O_4)$  orbital is a  $p$  orbital with occupancy 1.87e and is hyperconjugated with the  $\sigma^*$  antibonding orbital of the  $C_{12}-H$  bond, formed by the contribution of 40.22% of the  $sp^{2.12}$  hybrid orbital of the  $C_{12}$  atom with 59.78% of the orbital  $s$  of H. However, the  $C_{13}-H\cdots O_4$  interaction is stabilized only by the  $\eta_1(O_4) \rightarrow \sigma^*(C_{14}-C_{13})$

**Table 3.** Topological parameters were calculated for the CNP-OM and CNP-CL molecular interactions at the bond critical point

Interaction	H...A / Å	D - H...A / degree	$\rho_{BCP}^a$ / a.u.	$\nabla^2\rho_{BCP}^b$ / a.u.	$G(r)^c$ / a.u.	$v(r)^d$ / a.u.	$h(r)^e$ / a.u.	$\frac{G(r)}{ v(r) }$
CNP-OM								
$C_{28}-H\cdots O_1$	2.589	147.79	0.0058	0.0222	0.0045	-0.0035	0.0010	0.8
$C_9-H\cdots O_3$	2.464	142.67	0.0086	0.0308	0.0065	-0.0053	0.0012	0.8
$C_{15}-H\cdots O_3$	2.511	148.46	0.0075	0.0270	0.0056	-0.0045	0.0011	0.8
$C_{12}-H\cdots O_4$	2.591	124.85	0.0076	0.0283	0.0060	-0.0050	0.0011	0.8
$C_{13}-H\cdots O_4$	2.653	121.67	0.0066	0.0257	0.0054	-0.0044	0.0010	0.8
$C_8-H\cdots O_3$	2.366	155.04	0.0103	0.0390	0.0080	-0.0063	0.0017	0.8
$C_{19}-H\cdots O_6$	2.586	147.01	0.0062	0.0227	0.0047	-0.0038	0.0009	0.8
CNP-CL								
$C_{12}-H\cdots O_1$	2.528 <sup>f</sup>	135.40 <sup>f</sup>	0.0079	0.0297	0.0062	-0.0050	0.0012	0.8
$C_{13}-H\cdots O_2$	2.441 <sup>f</sup>	167.70 <sup>f</sup>	0.0091	0.0325	0.0067	-0.0054	0.0014	0.8
$C_{27}-H\cdots O_3$	2.655 <sup>f</sup>	164.08 <sup>f</sup>	0.0058	0.0193	0.0041	-0.0034	0.0007	0.8
$C_{19}-H\cdots O_5$	2.572 <sup>f</sup>	122.19 <sup>f</sup>	0.0075	0.0293	0.0061	-0.0049	0.0012	0.8
$C_{24}-H\cdots O_5$	2.591 <sup>f</sup>	136.78 <sup>f</sup>	0.0059	0.0197	0.0042	-0.0035	0.0007	0.8
$C_{25}-H\cdots O_6$	2.673 <sup>f</sup>	154.97 <sup>f</sup>	0.0059	0.0197	0.0042	-0.0035	0.0007	0.8

<sup>a</sup>Total electronic density on BCP; <sup>b</sup>Laplacian of electron density on BCP; <sup>c</sup>Lagrangian kinetic energy; <sup>d</sup>potential energy density; <sup>e</sup>total energy density; <sup>f</sup>reference 13.

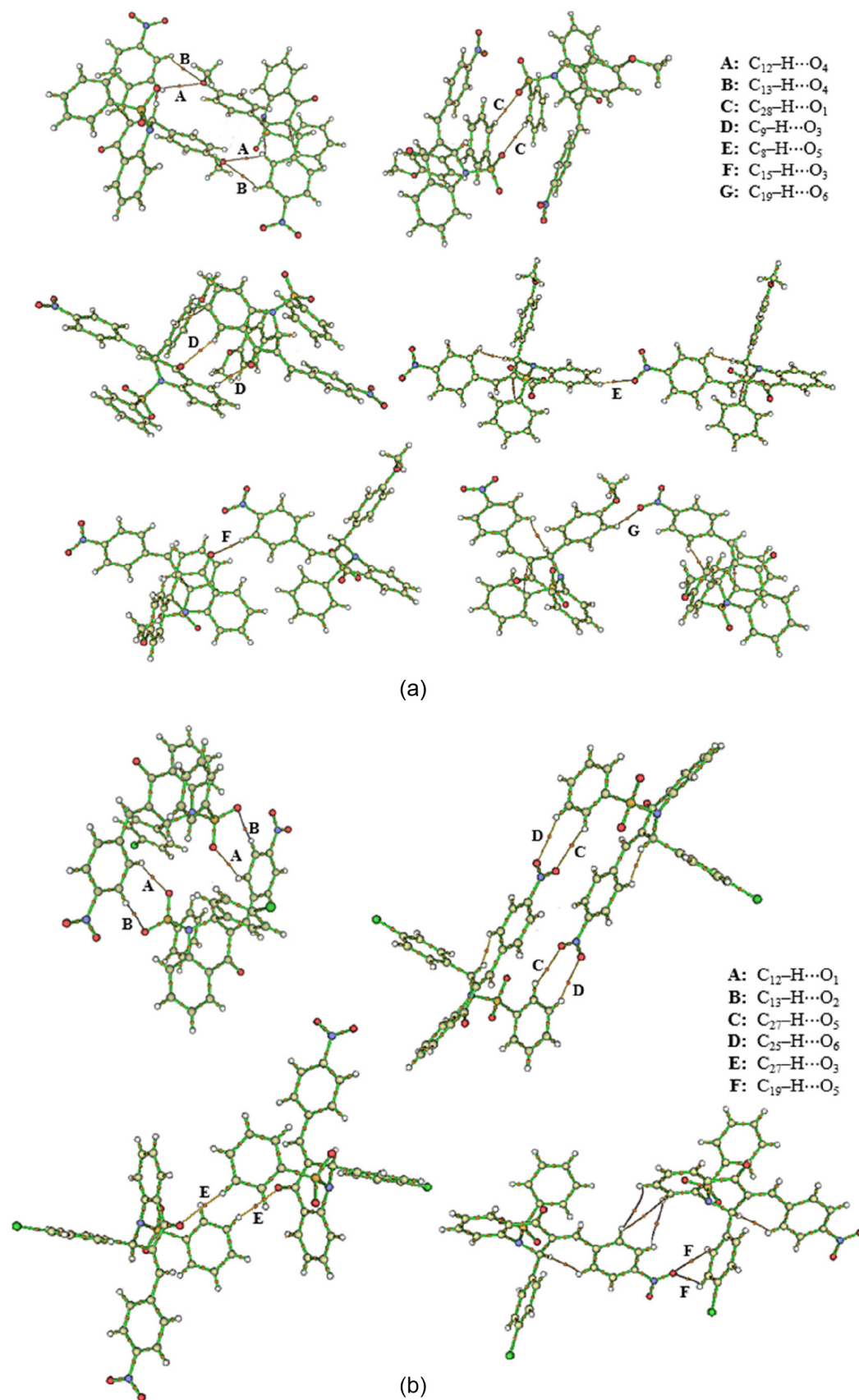


**Figure 13.** Molecular graphs of some BP of the intermolecular interactions in the supramolecular arrangements of the (a) CNP-OM and (b) CNP-CL quinoline-chalcones.

hyperconjugation, where the  $\sigma^*$  antibonding orbital is formed by 49.28% of the  $sp^{1.63}$  hybrid of the  $C_{14}$  atom and by 50.72% of the  $sp^{1.98}$  hybrid of the  $C_{13}$  atom, with occupancy 0.02e.

In the case of CNP-CL, the  $C_{12}-H\cdots O_1$  and  $C_{13}-H\cdots O_2$  interactions present in dimer 1 are formed by hyperconjugation of the lone pairs of the  $O_1$  atom with the antibonding  $\sigma^*$  orbitals of the  $C_{12}-H$  and  $C_{12}-C_{11}$  bonds, and the  $O_2$  lone pairs with the antibonding  $\sigma^*$  orbitals of the  $C_{13}-H$  and  $C_{12}-C_{11}$  bonds. For the formation of the  $C_{12}-H\cdots O_1$  bond, the hyperconjugations  $\eta_1(O_1) \rightarrow \sigma^*(C_{12}-H)$  and  $\eta_1(O_1) \rightarrow \sigma^*(C_{11}-C_{12})$  occur, where the values of  $E^{(2)}$  are 0.16 and 0.07 kcal mol<sup>-1</sup>, respectively. In this case,  $\eta_1(O_1)$  is formed by an  $O_1$   $sp^{0.40}$  hybrid orbital with occupancy 1.98e (this hybrid orbital has 71.26% s character *versus* only 28.73% p character); the antibonding  $\sigma^*$  orbital of  $C_{12}-H$  is formed by the contribution of 40,00% of the  $sp^{2.19}$  hybrid orbital of  $C_{12}$  and 60,00% of the s orbital of H. The  $C_{11}-C_{12}$  antibonding  $\sigma^*$  orbital is formed by 50.67% of the  $C_{12}$   $sp^{1.88}$  hybrid orbital and 49.33% of the  $C_{11}$   $sp^{1.89}$  hybrid orbital. The hyperconjugations  $\eta_2(O_1) \rightarrow \sigma^*(C_{12}-H)$  and  $(O_1) \rightarrow \sigma^*(C_{11}-C_{12})$  also occur, where the  $E^{(2)}$  values are 0.09 and 0.09 kcal mol<sup>-1</sup>, respectively, contributing even less to the stabilization of the H-bond for the dimer. Here, the  $\eta_2(O_1)$  lone pair is a pure p orbital with occupancy 1.83e. Finally, we observe the hyperconjugation  $\eta_3(O_1) \rightarrow \sigma^*(C_{12}-H)$  for the formation of the interaction, where the  $E^{(2)}$  value is 0.11 kcal mol<sup>-1</sup>, and the lone pair is also a p orbital with occupancy 1.80e. The  $C_{13}-H\cdots O_2$  interaction is formed by the hyperconjugations  $\eta_1(O_2) \rightarrow \sigma^*(C_{13}-H)$ ,  $(O_2) \rightarrow \sigma^*(C_{13}-H)$  and  $\eta_3(O_2) \rightarrow \sigma^*(C_{13}-H)$ , which contributes more to the stabilization of the H-bond in the dimer with  $E^{(2)}$  values equal to 0.13, 0.56, and 0.23 kcal mol<sup>-1</sup>, respectively. The lone pairs are formed by the  $O_2$   $sp^{0.39}$  hybrid orbital ( $\eta_1$ ) and by the  $O_2$  pure p orbitals ( $\eta_2$  and  $\eta_3$ ). The occupancies obtained for these orbitals are 1.98e, 1.82e, and 1.78e. The antibonding  $\sigma^*$  orbital of  $C_{13}-H$  is formed by 39.33% of the  $sp^{2.05}$  hybrid orbital of  $C_{13}$  and 60.67% of the s orbital of H. Hyperconjugation of the lone pair ( $O_2$ ) with the antibonding  $\sigma^*$  orbital of the  $C_{12}-C_{11}$  bond was also observed:  $\eta_2(O_2) \rightarrow \sigma^*(C_{12}-C_{11})$ , with  $E^{(2)} = 0.09$  kcal mol<sup>-1</sup>.

In Tables S1 and S2 (SI section), we present the hyperconjugations of the other interactions mentioned in Table 2. In addition to these, we observed weak hyperconjugation between the bonding  $\pi$  orbitals of the  $C_{20}-C_{19}$  bond and the antibonding  $\pi^*$  orbital of the  $C_{21}-C_{22}$  bond, where the  $E^{(2)}$  value is 0.09 kcal mol<sup>-1</sup>. This hyperconjugation justifies, in another way, the formation of the  $\pi \cdots \pi$  stacked interaction observed by the shape index of Figure 9. In this hyperconjugation, the  $\pi$  orbital has an

occupancy of 1.67e, being formed by 46.10% of the  $sp^{1.00}$  hybrid orbital of  $C_{20}$  and by 53.90% of the  $sp^{1.00}$  hybrid orbital of  $C_{19}$ , while the  $\pi^*$  orbital has an occupancy of 0.30e and is formed by 48.42% of the  $sp^{1.00}$  hybrid orbital of the  $C_{21}$  and 51.58% of the  $sp^{1.00}$  hybrid orbital of  $C_{22}$ .

The  $C_{28}-H$  and  $C_{24}-H$  bonds present in ring A are equivalent and interact with O atoms from different environments:  $O_1=S$  in CNP-OM and  $O_5=N$  in CNP-CL. Different quantities of hyperconjugation have been identified in both cases; whereas two occur in the first quinoline-chalcone, twice as many occur in CNP-CL. The sum of the stabilizing energies of these hyperconjugations gives stability to the interaction, which is approximately 1.3 times larger in CNP-CL. Likewise, the  $C_{12}-H$  bonds of the D ring interact with the  $O_4$  ether atom in CNP-OM and with  $O_1$  of the sulfonyl group in CNP-CL. While the sum of the  $E^{(2)}$  values obtained from the two hyperconjugations in CNP-OM are contrasted to the sum of the  $E^{(2)}$  values produced by the five hyperconjugations found in CNP-CL, the latter compound has almost twice the stability. The same happens in the case of the interactions of the  $C_{13}-H$  bonds with  $O_4$  (in CNP-OM) and  $O_2$  (in CNP-CL); however, hyperconjugations provide about 6.7 times more stability in CNP-CL. Finally, the interactions  $C_{19}-H\cdots O_6$  (in CNP-OM) and  $C_{19}-H\cdots O_5$  (in CNP-CL) are in the same environment, and, in this case, CNP-OM performs two hyperconjugations, resulting in an  $E^{(2)}$  value about 1.3 times greater than the single hyperconjugation observed in CNP-OM.

#### Molecular docking

The molecular docking method helps predict the interactions between small molecules and active sites in proteins at the atomic level so that the behavior of these structures at the binding site of the proteins can be elucidated as biochemical mechanisms.<sup>69</sup> Before docking analysis the octopine was redocking with the PBP, and RMSD (root mean square deviation) values (10 poses) were less than 1.0 Å. Docking analysis has shown that the CNP-OM appears to fit well in the binding site of the PBP (Figures 14a and 14b). A  $\pi$  stacking with TYR33A (distance = 3.5 Å) seems to play an essential role in the conformation of this chemical structure with the binding of the PBP. These results suggest that this compound could inhibit the *Agrobacterium tumefaciens*, which consists in an organism that transfers a T-DNA from the tumor-inducing plasmid into the plant cells.<sup>70</sup> *A. tumefaciens* is considered one of the most important plant pathogens, producing characteristic crown galls on numerous dicotyledonous plants.<sup>71</sup>

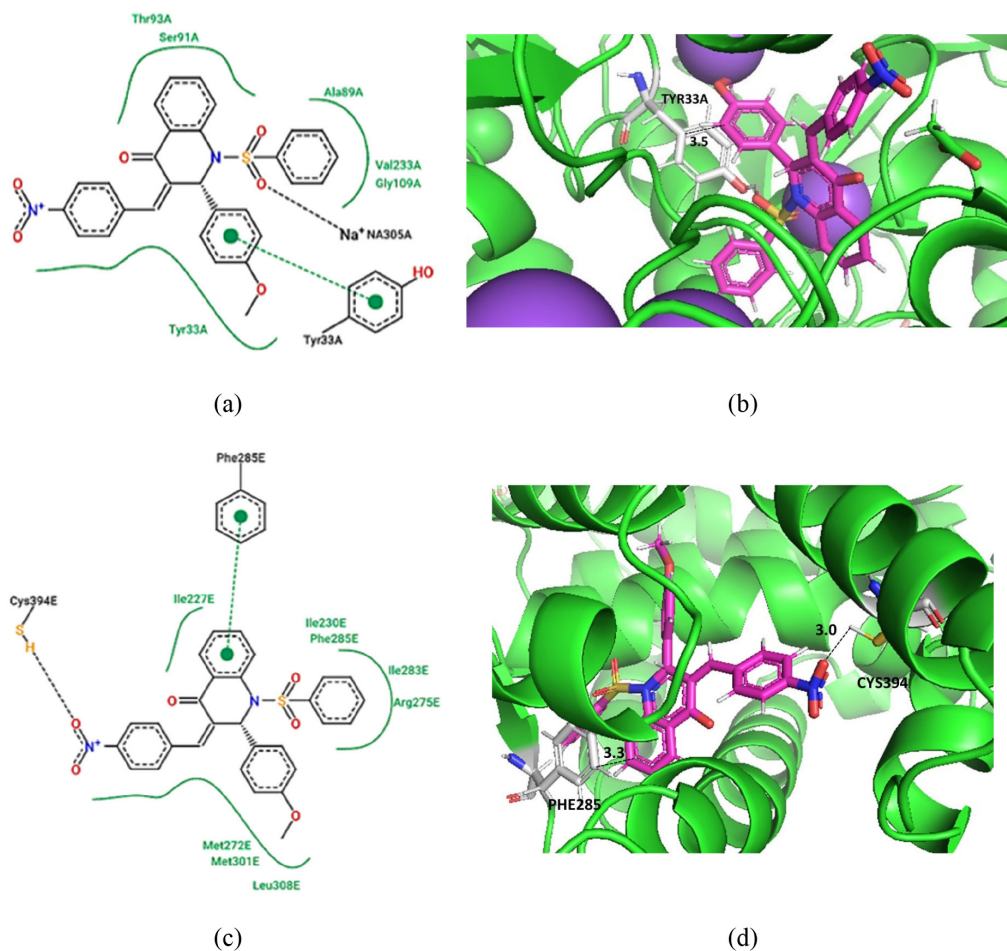


**Figure 14.** (a) 2D interaction map of CNP-OM to PBP in conformation 1. (b) CNP-OM docked in PBP active site in conformation 1. Distance values are in Angstroms. (c) 2D interaction map of CNP-OM to ecdysone receptor in conformation 1. (d) CNP-OM docked in ecdysone receptor in the binding site in conformation 1. Distance values are in Angstroms.

The docking analysis also suggested that the CNP-OM could interact with the active site of the ecdysone receptor. A  $\pi$  stacking with PHE285E seems to play an essential role in the conformation of this chemical structure with the binding (Figures 14c and 14d) of the target (distance = 3.3 Å). The ecdysone receptor is a hormone-dependent transcription factor. One reinforced hydrogen bond with CYS394 was the more intense interaction between the CNP-OM and the protein's binding site (distance = 3.0 Å). The ecdysone receptor is a hormone-dependent transcription factor that regulates the development and reproduction of arthropods.<sup>47</sup> This receptor is an important environmentally friendly target of other compounds (bisacylhydrazine insecticides), effective against Lepidoptera order.<sup>72-74</sup> The transcription factor is absent from mammals and is thus potentially useful as a safe insecticide target with more selective activity.<sup>72</sup> Thus, based on the results obtained in the two molecular docking analyses, the CNP-OM potential as a candidate substance to be applied to control pathogens and insects in agriculture is verified. In addition, the results obtained

corroborate analyzes previously carried out by Vaz *et al.*,<sup>13</sup> in which computational analyses presented similar targets for a structure similar to the one used in this work.

## Conclusions

Although CNP-OM and CNP-CL crystallized in different environments, no significant changes were observed in their molecular geometries, not even in their reactivity. The chemical descriptors showed that the CNP-OM molecule is slightly more reactive and more basic than CNP-CL. Such functional groups also did not change the nature of intermolecular interactions, in which the short-range contacts showed low intensity since the regions between the nuclear attractors have low charge density; that is, the electrons are depleted in the internuclear regions, so these are closed-shell interactions. Thus, the low  $\rho$  values, combined with the  $\nabla^2\rho > 0$  and  $h > 0$  values, lead to the conclusion that they are van der Waals interactions. However, the different substituted *para* groups on the

benzene ring resulted in different patterns of interactions in the supramolecular arrangement of the crystals. The docking studies of the CNP-OM quinoline-chalcone have shown potential pesticidal agent for its interaction and binding to amino acids in the ecdysone receptor and periplasmic binding protein active sites. These possible activities raise a perspective on the economic interest of testing this molecule *in vitro* and *in vivo* models.

## Supplementary Information

Crystallographic data (excluding structure factors) for the structures in this work were deposited in the Cambridge Crystallographic Data Centre as supplementary publication number codes 2241212 (CNP-OM) and 1981002 (CNP-CL). Copies of the data can be obtained, free of charge, via <https://www.ccdc.cam.ac.uk/structures/>.

Supplementary information from NBO analyses of the CNP-OM and CNP-CL quinoline-chalcone structures is found in Tables S1 and S2, as well as the CNP-OM infrared spectrum (Figure S1) and is freely available at <http://jbcbs.sbj.org.br> as a PDF file.

## Acknowledgments

This research was developed with the support of the Brazilian agencies: Fundação de Amparo à Pesquisa do Estado de Goiás (FAPEG), Conselho Nacional de Desenvolvimento Científico e Tecnológico (CNPq), and Coordenação de Aperfeiçoamento de Pessoal de Nível Superior (CAPES). Also, the authors thank the High-Performance Computing Center of the Universidade Estadual de Goiás (UEG).

## Author Contributions

Antônio S. N. Aguiar was responsible for the conceptualization, data curation, investigation, methodology, project administration, resources, writing-original draft, review and editing; João P. M. Rodrigues for the investigation, resources, writing-original draft, review and editing; Leonardo L. Borges for the data curation, methodology, resources, validation, writing-original draft, review and editing; Wesley F. Vaz for the formal analysis, investigation, resources, writing-original draft, review and editing; Giulio D. C. d'Oliveira for the conceptualization, investigation, resources, and writing-original draft; Caridad N. Perez for the conceptualization, data curation, formal analysis, investigation, methodology, resources, validation, writing-original draft, review and editing; Hamilton B. Napolitano for the conceptualization, data curation, formal analysis, methodology, project administration, supervision, validation, visualization, and writing-review and editing.

## References

1. Li, W.; Xu, F.; Shuai, W.; Sun, H.; Yao, H.; Ma, C.; Xu, S.; Yao, H.; Zhu, Z.; Yang, D.-H.; Chen, Z.-S.; Xu, J.; *J. Med. Chem.* **2019**, *62*, 993. [Crossref]
2. Mohamed, M. F. A.; Abuo-Rahma, G. E.-D. A.; *RSC Adv.* **2020**, *10*, 31139. [Crossref]
3. Coa, J. C.; García, E.; Carda, M.; Agut, R.; Vélez, I. D.; Muñoz, J. A.; Yepes, L. M.; Robledo, S. M.; Cardona, W. I.; *Med. Chem. Res.* **2017**, *26*, 1405. [Crossref]
4. Sashidhara, K. V.; Avula, S. R.; Mishra, V.; Palnati, G. R.; Singh, L. R.; Singh, N.; Chhonker, Y. S.; Swami, P.; Bhatta, R. S.; palit, G.; *Eur. J. Med. Chem.* **2015**, *89*, 638. [Crossref]
5. Guan, Y.-F.; Liu, X.-J.; Yuan, X.-Y.; Liu, W.-B.; Li, Y.-R.; Yu, G.-X.; Tian, X.-Y.; Zhang, Y.-B.; Song, J.; Li, W.; Zhang, S.-Y.; *Molecules* **2021**, *26*, 4899. [Crossref]
6. Ayalew, M. E.; *J. Biophys. Chem.* **2022**, *13*, 29. [Crossref]
7. Gaonkar, S. L.; Vignesh, U. N.; *Res. Chem. Intermed.* **2017**, *43*, 6043. [Crossref]
8. Praveen Kumar, C. H.; Katagi, M. S.; Nandeshwarappa, B. P.; *Chem. Data Collect.* **2022**, *42*, 100955. [Crossref]
9. Charris, J. E.; Monasterios, M. C.; Acosta, M. E.; Rodríguez, M. A.; Gamboa, N. D.; Martínez, G. P.; Rojas, H. R.; Mijares, M. R.; de Sanctis, J. B.; *Med. Chem. Res.* **2019**, *28*, 2050. [Crossref]
10. Dorababu, A.; Vijayalaxmi, S.; Sanjeevamurthy, R.; Vidya, L.; Prasannakumar, R.; Raghavendra, M. M.; *Bioorg. Chem.* **2020**, *105*, 104419. [Crossref]
11. Mirzaei, S.; Hadizadeh, F.; Eisvand, F.; Mosaffa, F.; Ghodsi, R.; *J. Mol. Struct.* **2020**, *1202*, 127310. [Crossref]
12. Ferreira, K. A. M.; Fontenelle, O. S. R.; Magalhães, E. A. F.; Bandeira, N. P.; Silva E. A.; de Menezes, J.; dos Santos, S. H.; *Rev. Virtual Quim.* **2018**, *10*, 1455. [Crossref]
13. Vaz, W. F.; Neves, B. J.; Custodio, J. M. F.; Silva, L. L.; D'Oliveira, G. D. C.; Lemes, J. A.; Lacerda, B. F. C.; Santos, S. X.; Perez, C. N.; Napolitano, H. B.; *J. Mol. Struct.* **2021**, *1226*, 129326. [Crossref]
14. Zhou, Z.; Kearnes, S.; Li, L.; Zare, R. N.; Riley, P.; *Sci. Rep.* **2019**, *9*, 10752. [Crossref]
15. Duarte, V. S.; Paula, R. L. G.; Custodio, J. M. F.; D'Oliveira, G. D. C.; Borges, L. L.; Pérez, C. N.; Perjesi, P.; Oliver, A. G.; Napolitano, H. B.; *J. Mol. Model.* **2022**, *28*, 176. [Crossref]
16. Cardona-G., W.; Yepes, A. F.; Herrera-R., A.; *Curr. Med. Chem.* **2018**, *25*, 3637. [Crossref]
17. Liu, M.; Khan, A.; Wang, Z.; Liu, Y.; Yang, G.; Deng, Y.; He, N.; *Biosens. Bioelectron.* **2019**, *130*, 174. [Crossref]
18. d'Oliveira, G.; Moura, A.; de Moraes, M.; Perez, C.; Lião, L.; *J. Braz. Chem. Soc.* **2018**, *29*, 2308. [Crossref]
19. de Castro, M. R. C.; Aragão, Â. Q.; da Silva, C. C.; Perez, C. N.; Queiroz, D. P. K. K.; Queiroz Jr., L. H. K.; Barreto, S.; de Moraes, M. O.; Martins, F. T.; *J. Braz. Chem. Soc.* **2015**, *27*, 884. [Crossref]

20. Sheldrick, G. M.; *Acta Crystallogr. A* **2015**, *71*, 3. [Crossref]
21. Sheldrick, G. M.; *Acta Crystallogr., Sect. C: Struct. Chem.* **2015**, *71*, 3. [Crossref]
22. Dolomanov, O. V.; Bourhis, L. J.; Gildea, R. J.; Howard, J. A. K.; Puschmann, H.; *J. Appl. Crystallogr.* **2009**, *42*, 339. [Crossref]
23. Hohenberg, P.; Kohn, W.; *Phys. Rev.* **1964**, *136*, B864. [Crossref]
24. Kohn, W.; Sham, L. J.; *Phys. Rev.* **1965**, *140*, A1133. [Crossref]
25. Frisch, M. J.; Trucks, G. W.; Schlegel, H. B.; Scuseria, G. E.; Robb, M. A.; Cheeseman, J. R.; Scalmani, G.; Barone, V.; Petersson, G. A.; Nakatsuji, H.; Li, X.; Caricato, M.; Marenich, A. v.; Bloino, J.; Janesko, B. G.; Gomperts, R.; Mennucci, B.; Hratchian, H. P.; Ortiz, J. v.; Izmaylov, A. F.; Sonnenberg, J. L.; Williams-Young, D.; Ding, F.; Lipparini, F.; Egidi, F.; Goings, J.; Peng, B.; Petrone, A.; Henderson, T.; Ranasinghe, D.; Zakrzewski, V. G.; Gao, J.; Rega, N.; Zheng, G.; Liang, W.; Hada, M.; Ehara, M.; Toyota, K.; Fukuda, R.; Hasegawa, J.; Ishida, M.; Nakajima, T.; Honda, Y.; Kitao, O.; Nakai, H.; Vreven, T.; Throssell, K.; Montgomery, J. A.; Peralta, J. E.; *Gaussian 16*, Revision C.01, 2016.
26. Zhao, Y.; Truhlar, D. G.; *Theor. Chem. Acc.* **2008**, *120*, 215. [Crossref]
27. Zhang, G.; Musgrave, C. B.; *J. Phys. Chem. A* **2007**, *111*, 1554. [Crossref]
28. Weinstein, H.; Osman, R.; Green, J. P.; Topiol, S. In *Chemical Applications of Atomic and Molecular Electrostatic Potentials*; Springer US: Boston, MA, 1981, p. 309-334.
29. Naray-Szabo, G.; Ferenczy, G. G.; *Chem. Rev.* **1995**, *95*, 829. [Crossref]
30. Cacialli, F.; Samorı, P.; Silva, C.; *MaterialsToday* **2004**, *7*, 24. [Crossref]
31. Atwood, J. L.; Gokel, G. W.; Barbour, L. J.; *Comprehensive Supramolecular Chemistry*, 2<sup>nd</sup> ed.; Elsevier: Amsterdam, 2017.
32. Spackman, M. A.; Jayatilaka, D.; *CrystEngComm* **2009**, *11*, 19. [Crossref]
33. Spackman, M. A.; McKinnon, J. J.; *CrystEngComm* **2002**, *4*, 378. [Crossref]
34. Turner, M.; McKinnon, J.; Wolff, S.; Grimwood, D.; Spackman, P.; Jayatilaka, D.; Spackman, M.; *CrystalExplorer17*, University of Western Australia, Western Australia, Australia, 2017.
35. Spackman, P. R.; Turner, M. J.; McKinnon, J. J.; Wolff, S. K.; Grimwood, D. J.; Jayatilaka, D.; Spackman, M. A.; *J. Appl. Crystallogr.* **2021**, *54*, 1006. [Crossref]
36. Hirshfeld, F. L.; *Isr. J. Chem.* **1977**, *16*, 198. [Crossref]
37. McKinnon, J. J.; Spackman, M. A.; Mitchell, A. S. A. S.; *Acta Crystallogr. B* **2004**, *60*, 627. [Crossref]
38. Bader, R. F. W.; *Acc. Chem. Res.* **1985**, *18*, 9. [Crossref]
39. Bader, R. F. W.; *Atoms in Molecules - A Quantum Theory*; Clarendon Press Publication: Ontario, 1994.
40. Lu, T.; Chen, F.; *J. Comput. Chem.* **2012**, *33*, 580. [Crossref]
41. Weinhold, F.; Landis, C. R.; *Discovering Chemistry with Natural Bond Orbitals*, 1<sup>st</sup> ed.; John Wiley & Sons, Inc.: USA, 2012.
42. Weinhold, F.; Landis, C. R.; *Chem. Educ. Res. Pract.* **2001**, *2*, 91. [Crossref]
43. Alabugin, I. V.; Gilmore, K. M.; Peterson, P. W.; *Wiley Interdiscip Rev Comput Mol Sci* **2011**, *1*, 109. [Crossref]
44. Verdonk, M. L.; Chessari, G.; Cole, J. C.; Hartshorn, M. J.; Murray, C. W.; Nissink, J. W. M.; Taylor, R. D.; Taylor, R.; *J. Med. Chem.* **2005**, *48*, 6504. [Crossref]
45. Vigouroux, A.; El Sahili, A.; Lang, J.; Aumont-Nicaise, M.; Dessaux, Y.; Faure, D.; Morera, S.; *Sci. Rep.* **2017**, *7*, 18033. [Crossref]
46. Carmichael, J. A.; Lawrence, M. C.; Graham, L. D.; Pilling, P. A.; Epa, V. C.; Noyce, L.; Lovrecz, G.; Winkler, D. A.; Pawlak-Skrzecz, A.; Eaton, R. E.; Hannan, G. N.; Hill, R. J.; *J. Biol. Chem.* **2005**, *280*, 22258. [Crossref]
47. Carmichael, J. A.; Lawrence, M. C.; Graham, L. D.; Pilling, P. A.; Epa, V. C.; Noyce, L.; Lovrecz, G.; Winkler, D. A.; Pawlak-Skrzecz, A.; Eaton, R. E.; Hannan, G. N.; Hill, R. J.; *J. Biol. Chem.* **2005**, *280*, 22258. [Crossref]
48. Stierand, K.; Rarey, M.; *ChemMedChem* **2007**, *2*, 853. [Crossref]
49. Stierand, K.; Maass, P. C.; Rarey, M.; *Bioinformatics* **2006**, *22*, 1710. [Crossref]
50. Universitat Hamburg PoseView Interface, <https://www.zbh.uni-hamburg.de/en/forschung/amd/server/poseview.html>, accessed in August.
51. Schrodinger Pymol Molecular Graphics System 2.0, <https://pymol.org/2/>, accessed in August.
52. Zhan, C.-G.; Nichols, J. A.; Dixon, D. A.; *J. Phys. Chem. A* **2003**, *107*, 4184. [Crossref]
53. March, N. H.; *J. Phys. Chem.* **1982**, *86*, 2262. [Crossref]
54. Parr, R. G.; Yang, W.; Hill, C.; Carolina, N.; *J. Am. Chem. Soc.* **1984**, *106*, 4049. [Crossref]
55. Chermette, H.; *J. Comp. Chem.* **1999**, *20*, 129. [Crossref]
56. Pearson, R. G.; *J. Am. Chem. Soc.* **1963**, *85*, 3533. [Crossref]
57. Pearson, R. G.; *J. Mol. Struct.: THEOCHEM* **1992**, *255*, 261. [Crossref]
58. Pearson, R. G.; *J. Chem. Sci.* **2005**, *117*, 369. [Crossref]
59. Janak, J. F.; *Phys. Rev. B* **1978**, *18*, 7165. [Crossref]
60. Parr, R. G.; Szentpaly, L. V.; Liu, S.; *J. Am. Chem. Soc.* **1999**, *121*, 1922. [Crossref]
61. Perez, P.; Domingo, L. R.; Jose Aurell, M.; Contreras, R.; *Tetrahedron* **2003**, *59*, 3117. [Crossref]
62. Domingo, L. R.; Aurell, M. J.; Perez, P.; Contreras, R.; *Tetrahedron* **2002**, *58*, 4417. [Crossref]
63. Fukui, K.; *Angew. Chem., Int. Ed.* **1982**, *21*, 801. [Crossref]
64. Fukui, K.; *Science* **1982**, *218*, 747. [Crossref]
65. Etter, M. C.; MacDonald, J. C.; Bernstein, J.; *Acta Crystallogr., Sect. B: Struct. Sci., Cryst. Eng. Mater.* **1990**, *46*, 256. [Crossref]
66. Bernstein, J.; Davis, R. E.; Shimoni, L.; Chang, N.-L.; *Angew. Chem., Int. Ed.* **1995**, *34*, 1555. [Crossref]

67. Bader, R. F. W.; Nguyen-Dang, T. T.; Tal, Y.; *Rep. Prog. Phys.* **1981**, *44*, 893. [Crossref]
68. Carroll, M. T.; Bader, R. F. W.; *Mol. Phys.* **1988**, *65*, 695. [Crossref]
69. Bitencourt-Ferreira, G.; de Azevedo, W. F. In *Docking Screens for Drug Discovery*, vol. 2053; Humana: New York, USA, 2019. [Crossref]
70. Pitzschke, A.; Hirt, H.; *EMBO J.* **2010**, *29*, 1021. [Crossref]
71. Mansfield, J.; Genin, S.; Magori, S.; Citovsky, V.; Sriariyanum, M.; Ronald, P.; Dow, M.; Verdier, V.; Beer, S. v.; Machado, M. A.; Toth, I.; Salmond, G.; Foster, G. D.; *Mol. Plant Pathol.* **2012**, *13*, 614. [Crossref]
72. Dhadialla, T. S.; Carlson, G. R.; Le, D. P.; *Annu. Rev. Entomol.* **1998**, *43*, 545. [Crossref]
73. Samantsidis, G.-R.; Fotiadou, M.; Tzavellas, S.; Geibel, S.; Nauen, R.; Swevers, L.; Denecke, S.; Vontas, J.; *Insect Biochem. Mol. Biol.* **2022**, *151*, 103830. [Crossref]
74. Shen, G.-M.; Chen, W.; Li, C.-Z.; Ou, S.-Y.; He, L.; *Pestic. Biochem. Physiol.* **2019**, *159*, 85. [Crossref]

Submitted: March 30, 2023

Published online: August 21, 2023